ACS Catalysis
Research Article
pubs.acs.org/acscatalysis

Nature of the N−Pd Interaction in Nitrogen-Doped Carbon Nanotube Catalysts

Rosa Arrigo,*[,†] Manfred E. Schuster,[‡] Zailai Xie,[‡] Youngmi Yi,[‡] Gregor Wowsnick,[‡] Li L. Sun,[‡] Klaus E. Hermann,[‡] Matthias Friedrich,[‡] Patrick Kast,[‡] Michael Hävecker,[§] Axel Knop-Gericke,[‡] and Robert Schlögl[‡,†]

[†]Max-Planck-Institut für Chemische Energiekonversion, Stiftstrasse 34-36, 45470 Mülheim an der Ruhr, Germany
[‡]Department of Inorganic Chemistry, Fritz-Haber-Institut der Max-Planck Gesellschaft, Faradayweg 4-6, 14195 Berlin, Germany
[§]Helmholtz-Zentrum Berlin für Materialien und Energie, BESSY-II Albert-Einstein-Straße 15, 12489 Berlin, Germany

Supporting Information

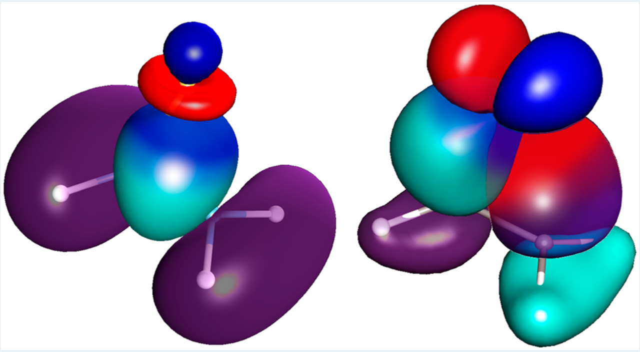

ABSTRACT: In this work, the geometric and electronic structure of N species in N-doped carbon nanotubes (NCNTs) is derived by X-ray photoemission (XPS) and absorption spectroscopy (NEXAFS) of the N 1s core excitation. Substitutional N species in pyridine-like configuration and another form of N with higher thermal stability are found in NCNTs. The structural configuration of the high thermally stable N species, in the literature often referred to as graphitic N, is assessed in this work by a combined theoretical and experimental study as a 3-fold substitutional N species in an NCNT basic structural unit (BSU). Furthermore, the nature of the interaction of those N species with a Pd metal center immobilized onto NCNTs is of σ-type donation from the filled π-orbital of the N atom to the empty d-orbital of the Pd atom and a π back-donation from the filled Pd atomic d-orbital to the π^* antibonding orbital of the N atom. We have found that the interaction of pyridine N with Pd is characterized by a charge transfer typical of a covalent chemical bond with partial ionic character, consistent with the chemical shift observed in the Pd 3d core level of divalent Pd. Graphitic N sites interact with Pd by a covalent bond without any charge redistribution. In this case, the electronic state of the Pd corresponds to metallic Pd nanoparticles electronically modified by the interaction with the support. The catalytic reactivity of these samples in hydrogenation, CO oxidation, and oxygen reduction reaction (ORR) allowed clarifying some aspects of the metal carbon support interaction in catalysis.

KEYWORDS: *NCNT, ORR, metal−support interaction, NEXAFS, graphitic N, DFT*

INTRODUCTION

The introduction of specific functional groups with electron acceptor or donor character at the periphery of conjugated polycyclic carbon structures enables tailoring their chemical properties[1−4] as well as electronic properties,[5] providing a multitude of design possibilities. Among all, N-doped nanocarbon is the preferred choice in the field of catalysis and electrocatalysis. In fuel-cells,[6,7] electrochemical CO_2 reduction,[8] liquid-phase selective oxidation catalysis,[9] H_2O_2 direct synthesis,[10] the common observation is the improved catalytic activity, selectivity, and stability of metal nanoparticles supported on N-doped nanocarbon with respect to the N-free counterpart.

Furthermore, a very intriguing aspect of the N-doped nanocarbon chemistry reported earlier by Boehm et al.[11,12] is that the substitutional N-functional groups at the periphery of the carbon layer enable metal-free catalysis. More recently, N-containing nanocarbon has attracted much attention in electrocatalysis due to the ability of N functional groups to modify the mechanism of the oxygen reduction reaction (ORR) on C from a 2e$^-$ transfer to a 4e$^-$ transfer mechanism.[6,7]

A variety of N chemical configurations are possible in graphite-like materials; among these, there is a general observation that the substitutional N species are beneficial. This includes N species whose chemical properties differ substantially,[13] such as pyridine-like N, pyrrole-like N, and quaternary or graphitic N.[14] Pyridine N is a 2-fold coordinated N at the edge or in vacancies of the graphitic domains contributing to the π system with one p-electron. The lone pair of the N atom determines the basic character. Pyrrole is a 3-fold coordinated N atom in a pentagonal ring. Substituted in graphene, pyrrole is an electron localizer behaving as 2-position nucleophile. The structure of graphitic N is still matter of debate. Theoretical studies describe this species as a 3-fold

Received: January 18, 2015
Revised: March 13, 2015
Published: March 16, 2015

DOI: 10.1021/acscatal.5b00094
ACS Catal. 2015, 5, 2740−2753

Table 1. Chemical–Physical Properties

	Pd (wt %)		N (wt %)			BET	50% burn off		
samples	bulk[a]	surf[b]	bulk[a]	surf[b]	M[a] wt %	surf[b]	°C	ASA[d] (m^2/g)	D (%)/dp (nm)
NCNT	-	-	5.7 ± 0.2	5.7	7.3 ± 0.2	196	380	-	-
HT1000NCNT	-	-	2.4[c]	3.1	6.4 ± 1	178	400	-	-
HT1300NCNT	-	-	0.7[c]	0.7	6.4 ± 0.2	206	640	-	-
Pd1%NCNT	0.9 ± 0.1	2.45	5.9 ± 0.5	6.4	8.3 ± 0.3	-	-	nd	nd
Pd1%HT1000NCNT	0.8 ± 0.2	2.11	3.6 ± 0.5	2.3	7.3 ± 0.9	-	-	0.97	22/5.2
Pd0.3%HT1300NCNT	0.2 ± 0.1	2.07	1.7 ± 0.4	0.8	8 ± 0.3	-	-	0.35	26/4.2

[a] Bulk composition of M (Mn, Co, Si, Al) determined by EDX analysis on low magnification SEM images. [b] Surface composition determined by XPS assuming homogeneous model distribution (uncertainty in quantitative analysis by this method is of 10%–20%).[45] [c] EELS quantification. [d] Active surface area (ASA), dispersion (D), and average particle size (dp) determined by CO chemisorption. The notation "nd" indicates an experiment which did not produce measurable CO chemisorption.

coordinated N atom replacing a C atom in a planar configuration.[15] However, in virtue of its X-ray photoemission spectroscopy N 1s core-level chemical shift, this species is also ascribed to a positively charged tetrahedric N atom intermolecularly interacting with anionic functional groups.[16] The controversy originates from the fact that N substitution in the BSU[17] of graphene is not energetically favorable and out-of-plane deformation results in structure stabilization.[18,19] The difficulty of incorporating N into a carbon lattice is well exemplified by the search for the elusive C_3N_4[20,21] and the discovery of the m-C_3N_4[22] where defects in a continuous lattice of carbon accommodate N atoms.

The effect of the presence of substitutional N doping was studied in the literature theoretically and experimentally on different model systems: graphene, small single-wall nanotubes,[18,23] and amorphous carbon nitrides.[19,24] The introduction of N induces localization of π states near the Fermi level around the defective site with charge redistribution between the N atom and the neighboring C atoms.[24,25] The activation of O_2 in ORR over N-doped nanocarbon is attributed to localized electron-enriched N defective states.[26,27] Recently, doping of carbon with B was also shown to be a suitable alternative to realize metal-free catalysts for ORR.[28,29] Therefore, independently of the type of doping heteroatom, the induced redistribution of charge with local depletion and accumulation facilitates intermolecular charge transfer reactions with a substrate molecule. In a conceptual study, it was found that defects in graphene tend to localize charge near the missing atom leading to the formation of radicals that gave rise to the formulation of "spin catalysis".[30] Electron spin density redistribution has been also reported to strongly affect the formation of intermediate molecules in ORR.[31]

N-defective sites are also involved in interaction with immobilized metal nanoparticles.[32] In this respect, the method of the metal immobilization plays an important role. In fact, for evaporated Pd and Pt,[33−35] O-containing vacancies act as nucleation centers for metal clusters through a weak interaction which does not involve any covalent bonding but only charge transfer at the interface. In contrast, the interaction of Pd with oxidized carbon support prepared via impregnation occurs through a covalent bond to C atoms neighboring O atoms.[34,36] Zhou et al.[37] predicted that Pt atoms decorate the B- or N-doped carbon nanotubes surface through covalent bond with C neighboring N and B atoms.

We have reported on the Pd- on N-doped carbon nanotubes (NCNTs) system for several catalytic applications.[9,10] The high affinity of Pd to form σ or π bonds with C, but also with N-containing ligands, leads to a large variety of chemical species in analogy to Pd(0) and Pd(II) organometallic complexes.[38,39] HRTEM studies have evidenced that the nanoparticles wetting at the NCNTs surface resents of the strength of the metal support interactions and influences the particle morphology. "Raft-like" nanostructured metal coexists with spherical particles in systems such as Pd/NCNTs catalyst.[9,10] The doping of CNT with N enables an electronic modification of the immobilized Pd that determines the reactivity profile in the direct H_2O_2 synthesis. In fact, only a small portion of metal nanoparticles is stabilized at longer reaction times, while most of the nanoparticles undergo morphological modifications, which influences the catalytic performance negatively. This indicates that only a minority of defective sites on the graphitic support enables strong interactions.

Despite the growing literature on the application of NCNTs for catalysis and electro-catalysis, understanding the role of the N species is still phenomenological.[17] Little attention was given to rationalize the nature of the interaction at the metal/support interface in terms of reactivity implications with few studies available.[37,40]

Herein we discuss the implication of the Pd/N bonding state on the reactivity of Pd nanoparticles on N-doped CNT toward O and H in redox reaction for catalysis and electro-catalysis with the aim to provide a broad overview on the reactivity of these materials.

We report a NEXAFS and XPS study aimed to elucidate bonding of N species in NCNT and the nature of the coordination of Pd at the different N sites. The nature of the samples and their preparation was rationally chosen to induce the desired chemical interaction between the metal center and each type of N species and to observe them singularly. For this purpose, the different thermal stability of the N species have been exploited to produce, via thermal annealing of NCNTs, a set of samples with a different population of N species, subsequently used to immobilize Pd. Pd particle dispersion was qualitatively studied by means of HRTEM and HAADF-STEM, while CO chemisorption determined quantitative dispersion and exposed metal surface area. Additionally, quantum chemical calculations on local CNT sections were carried out to determine electronic core excitations of substitutional nitrogen.

The catalytic systems studied are the liquid-phase hydrogenation of phenyl acetylene, the CO oxidation, and the ORR. The study presented here provides relevant insights toward the rational synthesis optimization of application-adapted N-doped carbon nanostructures.

EXPERIMENTAL SECTION

Synthesis of Pd-Containing Samples. In this work, NCNTs provided by Bayer Technology Service were used. Those NCNTs are obtained via catalytic chemical vapor deposition (CCVD) of a N-containing C precursor[41] using spinel type Co−Mn mixed oxide catalyst[42] studied and developed further in the CarboScale project within the Innovation Alliance Carbon Nanotube.[43,44] In this successful research, it was found that the incorporation of the active phase (Co) directly into an oxide matrix containing Mn, from which can also be easily extracted to sinter and to form the desired metal nanoparticles at the temperature coinciding with the CNT nucleation temperature, enables yield and homogeneity in diameter and structure of the grown CNTs far greater than those obtained with other catalysts. The TEM and SEM images of the as-received NCNTs are reported in Figures S1 and S2.

They contain impurities from the CNT growing catalyst such as Mn, Co, Al, and Mg accounting for the 8% in weight (Table 1).Those impurities are not immobilized on the NCNT surface, but they are agglomerated apart from the nanotubes, which appear in HRSEM images very clean and only few metal particles occur to be encapsulated in the inner tube of the NCNTs (Figure S2c,d).

In the present work, carried out also as part of the CarboScale project, the pristine nanotubes were annealed at 1000 °C (HT1000NCNT) or 1300 °C (HT1300NCNT) in Ar for 4 h to selectively remove pyridine N species and retain most thermally stable N species. HRTEM images of the three samples are reported in Figure S3. The complete characterization of the nanotubes including elemental analysis, BET surface area and temperature of 50% burn off are reported in Table 1. The BET surface area remains similar after the thermal treatments of the NCNTs, but the annealing increases their thermal stability as indicated by the increase of the temperature of 50% burn off. The three NCNT carrier samples were used to immobilize palladium via incipient wet impregnation method. The NCNT, HT1000NCNT, and HT1300NCNT were impregnated with an aqueous solution of $Pd(NO_3)_2$ (10 mL/g cat). For this purpose, the required volume of a commercial solution of $Pd(NO_3)_2$ (Sigma-Aldrich 8.5% Pd wt/wt) was added to a 0.01 M HNO_3 solution and dropwise added to the NCNT. The metal loading was 1% (w/w) for NCNT and HT1000NCNT and 0.3% (w/w) for the HT1300NCNT. The slurry was then sonicated in a ultrasonic bath for 10 s, and afterward, the solvent was evaporated slowly at room temperature in air for 48 h. Thereafter, the samples containing the metal precursor were oxidized in 5% O_2 at 200 °C for 2 h and reduced in 5% H_2 at 200 °C for 2 h. Those samples are referred to as Pd1%NCNT, Pd1%HT1000NCNT, and Pd0.3% HT1300NCNT. The sample notation and the Pd loading of the Pd catalysts as determined by EDX analysis are reported in Table 1.

To evaluate the impact of the reactive atmosphere on the electronic structure of the NCNT apart from the metal coordination, a "blank" NCNT sample was prepared as well, following the same recipe as for the PdNCNT sample, but without the use of the metal precursor.

In addition, NCNT, HT1000NCNT, and HT1300NCNT samples were impregnated with an aqueous solution of Na_2PdCl_4 (10 mL/g cat). For this purpose Na_2PdCl_4 from Aldrich (99,99% purity) was dissolved in diluted HCl (0.01M) to obtain a catalyst with metal loading of 2 wt %/wt for NCNT and HT1000NCNT and 1 wt %/wt for HT1300NCNT. Those samples are referred to as $PdCl_2$NCNT, $PdCl_2$HT1000NCNT and $PdCl_2$HT1300NCNT.

Na_2PdCl_4 was chosen because in acidic media it allows the favorable interaction between the resulting positive nitrogen atoms on the NCNT and negative $PdCl_4^{2-}$ species in solution. The slurry was then sonicated in an ultrasonic bath for 10 s, and afterward, the solvent was evaporated slowly at room temperature in air for 48 h. A Pd1%HT1300NCNT sample was also prepared starting from $PdCl_2$HT1300NCNT$^-$ precursor by oxidation in 5% O_2 at 200 °C and reduction in 5% H_2 at 200 °C. Another "blank" HT1300NCNT sample was prepared by impregnation with 0.01 M HCl to study the interaction between nitrogen and Cl. Blank and precursor-containing samples represent references to evaluate the interaction at the N sites from a spectroscopic point of view. A total of eight samples were prepared to investigate all possible interactions (Pd/N, N/Cl, N/O, Pd^{2+}/N).

The samples notation and the corresponding preparation procedure are summarized in Table S1. Information about experimental conditions of the catalytic tests and the characterization techniques are reported in Supporting Information.

Theoretical Details. Geometric properties and electronic core excitations of substitutional nitrogen in the nitrogen functionalized CNTs are examined theoretically by quantum chemical calculations on local CNT sections. These include finite CNT rings of different width where dangling bonds at the CNT ring edges are saturated by hydrogen. Nitrogen doping is achieved by replacing central carbon atoms by nitrogen. As an example, Figure 1 shows the geometric structure of the largest N-doped CNT(11,0) ring, $N_2C_{64}H_{22}$, for which the numerical results will be discussed below. The NCNT rings are geometry optimized and corresponding equilibrium ground states are determined within density-functional theory (DFT) using the cluster code StoBe.[46] In addition, nitrogen core ionized states are calculated for $N_2C_{64}H_{22}$ in its equilibrium geometry to yield corresponding N 1s core ionization potentials (IP) in the NCNT ring to be compared with experimental X-ray photoemission (XPS) data. Further, core excited states are evaluated to yield final states for the N 1s core excitation spectrum to be compared with experimental X-ray absorption (NEXAFS) spectra. Here a different basis set is used for the core excited/ionized nitrogen center, IGLO-III type[15] in order

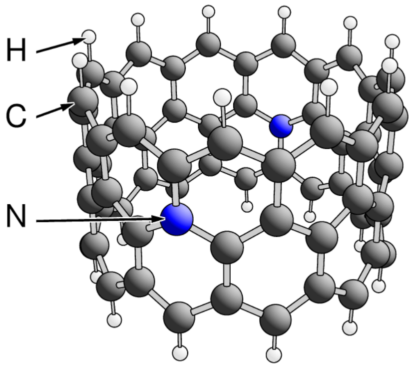

Figure 1. Geometric structure of a carbon nanotube (11,0) section functionalized by nitrogen and modeled by a $N_2C_{64}H_{22}$ cluster, see text. Atoms are shown by shaded balls of different color and labeled accordingly.

to adequately describe inner shell relaxation effects, see also ref 47. In all DFT calculations, the gradient corrected revised Perdew−Burke−Ernzerhof (RPBE) exchange−correlation functional[48,49] is employed.

Starting from a $C_{64}H_{22}$ CNT ring in its equilibrium geometry, the substitution of two central carbon atoms by nitrogen, thus keeping inversion symmetry, see Figure 1, and fixing the peripheral saturator hydrogen atoms yields the $N_2C_{64}H_{22}$ NCNT ring. Here the carbon coordinates differ very slightly from those of the $C_{64}H_{22}$ CNT ring (variations below 0.01 Å), and the nitrogen center moves outside by only 0.02 to 0.05 Å from its initial carbon position. Thus, functionalization by nitrogen does not lead to major structural changes due to rehybridization, which is also found in test studies of doped graphene flakes.

The computation of a self-consistent N 1s core hole state of the functionalized NCNT ring in its equilibrium geometry yields a total energy $E_{tot}(\text{NCNT; N 1 s}^{-1})$, which can be compared with that of the ground state, $E_{tot}(\text{NCNT; GS})$, where the difference defines the fully relaxed ionization potential $\text{IP}_{rlx}(\text{N 1s})$ of the N 1s electron according to

$$\text{IP}_{rlx}(\text{N}_{1s}) = E_{tot}(\text{NCNT; N}_{1s}{}^{-1}) - E_{tot}(\text{NCNT; GS}) \qquad (1)$$

which can be compared with experimental data from X-ray photoemission.

Theoretical N 1s NEXAFS spectra of the NCNT are computed by evaluating all core excited final states with corresponding transition energies and dipole transition matrix elements within the transition potential approach[50] in combination with a double basis set technique.[51] Transition energies and matrix elements are then convoluted using Gaussian broadening of varying width to simulate instrumental, vibrational, and lifetime effects. A full width at half-maximum (fwhm) value of 0.9 eV is applied below the ionization threshold while the broadening is increased linearly to 4 eV up to 10 eV above threshold. The resulting theoretical excitation spectrum is shifted rigidly to account for incomplete electronic relaxation in the transition potential approach as well as for relativistic effects to arrive at the final theoretical spectrum to be compared with measured NEXAFS data, see below. For further details of the method consult refs 50−54.

RESULTS AND DISCUSSION

Structural Characterization of the Supports. The C 1s core excitation EELS spectra of pristine NCNT and annealed HT1000NCNT and HT1300NCNT are (Figure 2) compared to HOPG considered as reference for an sp^2 hybridized carbon structure without in-plane defects. The spectra have been normalized to the σ^* resonance for comparison after power-law background subtraction. The C 1s core excitation spectrum of the NCNT exhibits features typical for graphite-like material. The π^* resonance at around 285.6 eV and the σ^* resonance at around 292 eV, originates from the electron excitation from the 1s core level to the π^* antibonding and σ^* antibonding orbitals of the C═C bond (in the ring), respectively. The spectral features between 286 and 290 eV are assigned to the Rydberg transitions, which are C 1s-π^* transition for C—R bond where R is a N, H, or O atom characteristic for functionalized aromatic groups.[56] Deviations from the structural order of HOPG produces a decrease in the ratio of the π^*/σ^* signal. Curvature of the graphene sheets produce also a shift of the π^* resonance to higher energy, which is observed as broadening of the resonance when an heterogeneous chemical bond configuration is present as seen for all the NCNT samples. Also the fine structure above 290 eV, observed in graphite, is not so well-defined in the case of the NCNT as a consequence of the higher disorder. Moreover, the Rydberg transition region is more intense for all the carbon nanotubes samples in comparison with HOPG indicating a higher amount of functional groups. C 1s core excitation EELS spectra show that the thermal treatment enhances the graphitic character. This is observed as an increase of the π^* resonance from NCNT to HT1300NCNT while a decrease of the Rydberg transition intensity from HT1000NCNT to HT1300NCNT indicates the loss of functional group as also observed in the N 1s core excitation EELS spectra in the black inset of Figure 2.

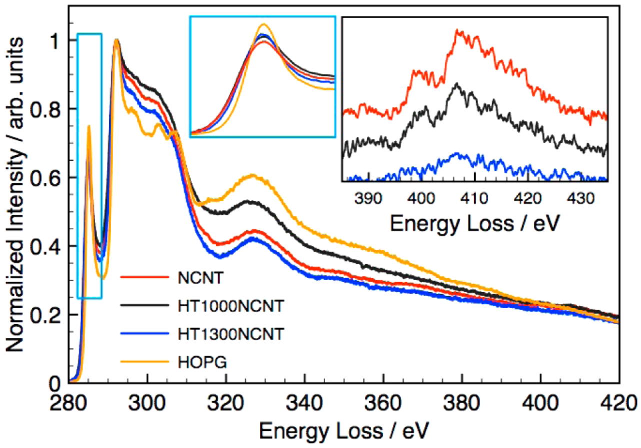

Figure 2. Magic-angle[55] C 1s core excitation EELS spectra for NCNT (red curve); HT1000NCNT (black curve); HT1300NCNT (blue curve) and HOPG (orange); Insets: N 1s EELS spectra (black-border inset) and detail of the π^* resonance (blue-border inset).

The quantification of the N abundance from the EELS spectra was 3.8 atom % for NCNT, 2.4 atom % for HT1000NCNT, and 0.7 atom % for HT1300NCNT. Increased graphitic ordering of the graphitic layers is consistent with an increase of the temperature of 50% burn off, which is very pronounced upon annealing at 1300 °C, as summarized in Table 1. The experimental C 1s core excitation NEXAFS spectra presented in Figure 3 offers additional information. Beside the enhancement of the intensity of the π^* resonance (Figure 3), additional structures are observed in the spectra. A prepeak to the π^*resonance is observed and assigned[56] to edge states appearing at the zigzag edge of graphite. Furthermore, the resonance at higher energy than the main π^* resonance is probably a localized high thermally stable CN bonding feature (inset in Figure 3). The N 1s NEXAFS spectra of the NCNT, HT1000NCNT, and HT1300NCNT samples in TEY are shown in Figure 4. The spectra are characterized by three resonances R1, R2, R3 between 399 and 402 eV, which are caused by 1s → π^* electronic transition for N atoms in N−C bonds. The resonance due to 1s→ σ^* transition is found above 408 eV (R4). The R1, R2, and R3 resonances occur at 398.8, 399.9, and 401.4 eV, respectively. The N 1s NEXAFS spectra resemble those previously reported for CN_x structures. The R1 resonance at 398.8 eV has been assigned to nitrogen atoms with two carbon neighbors in pyridine-like environment; and the resonance R3 at 401.4 eV to 3-fold nitrogen bonded to carbon.[57,58] The R2 resonance could be due to pyridine like orbital splits. Additionally, the C−N single bond in aniline-like

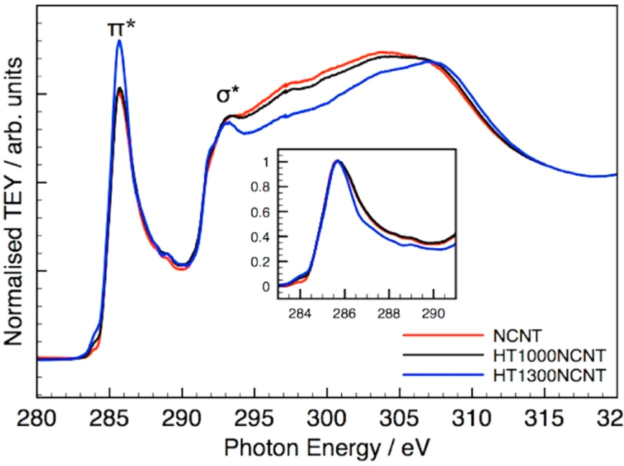

Figure 3. TEY C 1s core excitation NEXAFS spectra for NCNT (red curve); HT1000NCNT (black curve); HT1300NCNT (blue curve) and HOPG (green); detail of the normalized π^* resonance in the inset.

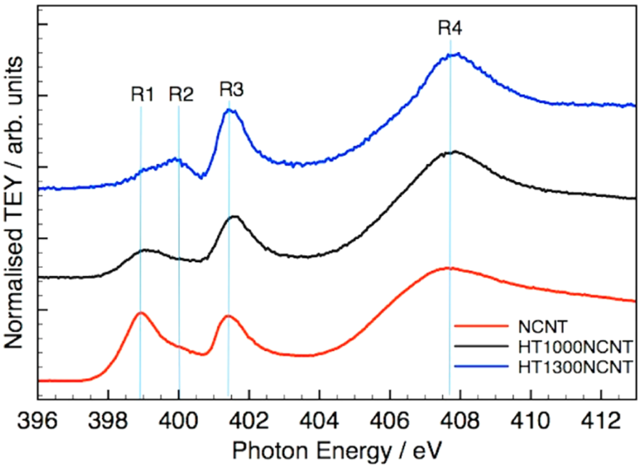

Figure 4. N 1s core excitation NEXAFS spectra for NCNT (red curve); HT1000NCNT (black curve); HT1300NCNT (blue curve). The spectra were collected in the total electron yield mode (TEY).

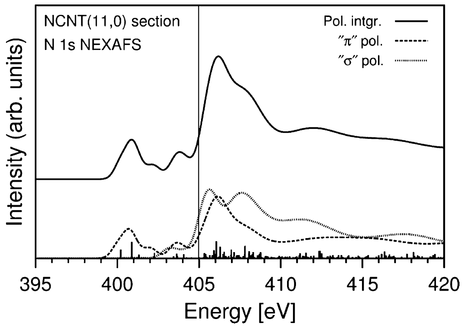

Figure 5. Theoretical N 1s core excitation spectra for the $N_2C_{64}H_{22}$ cluster representing a functionalized carbon nanotube (11,0) section, see text. The vertical line at 405.0 eV indicates the computed ionization threshold. The vertical lines of varying lengths corresponding to excitation probabilities denote the computed discrete excitation energies.

moieties or nitrile groups may contribute to the R2 resonance.[58,59] As the temperature of annealing increases, the nitrogen is driven out of the bonded matrix. In fact the thermal treatment of the N-CNT at 1000 °C leads to a decrease in the R1 resonance intensity associated with pyridine-like N. By further heat treatment at 1300 °C, both R1 and R3 resonances further decrease; however, resonance R3 is the dominant species. This thermally stable N species is referred to in literature as quaternary N or graphitic N.

The geometric property of this species is clarified by the electronic core excitation calculation here following. Figure 5 shows theoretical N 1s core excitation spectra of the functionalized carbon nanotube (11,0) section. The topmost spectrum (full line), labeled "Pol. intgr." in the figure, gives the total polarization-integrated spectrum. This spectrum is dominated by two major peaks at 400.9 eV below and 406.3 eV above ionization threshold (405.0 eV, indicated by a vertical line) with minor intensity structure in between. The core excitations yielding the main peaks involve, apart from the N 1s orbital, corresponding final state orbitals, which can be described by orbital analyses in the calculations. As a result of the dipole selection rules, the final state orbitals must contain N 2p character at the excitation center to yield finite transition probability where 2pz-, 2px-, and 2py-type contributions can occur. These can be distinguished in polarization-resolved excitation spectra, which are shown at the bottom of Figure 5. The spectrum labeled "π" pol. (dashed line) describes a polarization-resolved spectrum for the polarization vector perpendicular to the NCNT axis (i.e., perpendicular to the nanotube wall). Here only excitations involving final state orbitals with admixtures of N 2p perpendicular to the wall contribute to the spectrum and are found to dominate the low-energy peak of the total spectrum. The corresponding orbitals contain a nodal surface perpendicular to the wall which, in the case of planar geometry, would correspond to π-type final state orbitals and is only slightly perturbed by the curvature of the nanotube, hence the notation "π" pol. in Figure 5. On the other hand, the spectrum labeled "σ" pol. (hatched line) refers to a polarization averaged spectrum for the photon beam direction perpendicular to the NCNT axis. Here only excitations involving final state orbitals with admixtures of N 2p along the nanotube wall contribute to the spectrum. They mediate directed N−C coupling and dominate the high-energy peak of the total spectrum. The corresponding orbitals characterize bonding/antibonding along the nanotube wall which, in the case of planar geometry, would correspond to σ-type final state orbitals, hence the notation "σ" pol. in Figure 5. Thus, the final state orbital analysis of the polarization-resolved excitation spectra provides a clear distinction between the two major peaks in the total spectrum, ∼π- at lower and ∼σ-type at higher energy.

Figure 6 compares the experimental NEXAFS spectrum obtained for the HT1300NCNT system with the theoretical total N 1s core excitation spectrum of the functionalized carbon nanotube (11,0) section where absolute energy scales without adjustment have been used. Obviously, the two major peaks of the theoretical spectrum suggest an explanation for the two measured peaks at 401.5 eV (denoted R3) and 408.0 eV (denoted R4[12,60−63]) as ∼π- and ∼σ-type, respectively. The experimental peak separation amounts to 6.3 eV, rather similar to the theoretical value of 5.8 eV, and even better agreement between theory and experiments can be reached by shifting the theoretical spectrum by about 1.2 eV. The shift, which may be due to electrostatic effects and influence of the support in experiment, is quite reasonable considering the approximate description of the real nanotube system studied by experiment.

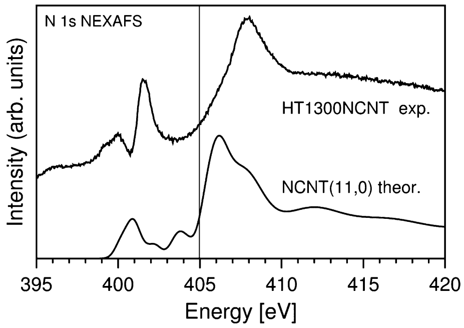

Figure 6. Comparison of the experimental N K-edge NEXAFS spectrum for the HT1300NCNT system (upper curve) with the theoretical N 1s core excitation spectrum of a functionalized carbon nanotube (11,0) section (lower curve, see Figure 5). The vertical line at 405.0 eV indicates the computed ionization threshold.

Further, the experimental spectrum shows a smaller peak structure (denoted R1, R2), which does not appear in the theoretical spectrum. This can be explained by the fact that in the experiment different types of nitrogen have been identified, for example, by XPS (Figure 7), which are not accounted for by the model calculations focusing only on substitutional nitrogen. On the other hand, the small peak structure between the two major peaks in the theoretical spectrum, which is missing in the experimental spectrum, may also be a consequence of the approximate nature of our model. The N 1s core level XP spectra of NCNT are presented in Figure 7 together with their species decomposition. The spectra are characterized by five different components:[64] the first peak at 398.5 eV refers to the pyridine-like N atoms (N1); the second peak at 399.2 eV (N2) is NH bonds in low thermally stable N species such as amide and amine. This component is present in small amount on the fresh NCNT. The third peak (N3) at 400.2 eV refers to N atoms in pyrrole-like configuration. The fourth component at around 401 eV (labeled as N4) is usually referred to any form of quaternary nitrogen (N4) including substitutional nitrogen and quaternary N due to intra or intermolecular hydrogen bond with pyridine or aniline functions. Furthermore, a peak with a binding energy shift of 402−403 eV is assigned to pyridine oxide (N5).

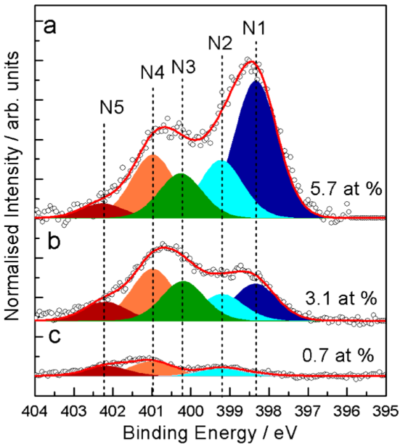

Figure 7. N 1s core-level spectra for (a) NCNT; (b) HT1000NCNT; (c) HT1300NCNT.

The thermally annealed HT1000NCNT and HT1300NCNT reveal a modified distribution of N species after the thermal treatment, which is dominated by the N4 components. A correspondence between the N1 component in the N 1s XPS and R1 in the N 1s NEXAFS among the samples exists, as well as between the N4 in the XPS and R3 in the NEXAFS. The HT1300NCNT shows no N1 component in the XPS while it still contains N2; correspondingly the R2 resonance is also observed, and therefore, the R2 resonance can be assigned to a specific C−N functionality rather than to splitting of state for the species related to the R1 resonance. The binding energy difference is similar in the experimental N 1s XPS and N 1s NEXAFS (Figure S5) in agreement with the building block model of the 1s core-excitation proposed by Stöhr.[65]

The computation of the fully relaxed ionization potential IP_{rlx}(N 1s) of the N 1s electron in the functionalized NCNT ring according to (1) yields a numerical value of 405.0 eV, which refers to absolute ionization energy. In the XPS experiments, see Figure 7, the energy scale of the different ionization peaks identified between 398 and 402 eV refers to the Fermi energy rather than to absolute ionization energy. Thus, for a comparison with the theoretical value, the experimental IP peak values need to be corrected by adding the work function of the CNT compound where a value of 4.68 eV is measured for HT1300NCNT, as described in the experimental section in Supporting Information. This leads to an absolute IP value of 404.88 and 405.68 eV for the peak labeled N3 and N4, respectively, in Figure 7, which are very close to the theoretical result, 405.0 eV. Thus, although the theoretical treatment cannot clearly differentiate between N3 and N4, experiments suggest peak N4 to originate from ionization of substitutional nitrogen in the CNT system.

Using tabulated theoretical photoelectron cross sections,[66] the chemical abundance of N functional groups on the NCNT surface was determined from XPS measurements and is reported in Table 1. The overall N abundance is significantly decreased after the thermal treatment. This is consistent with our previous study on the thermal stability of N species in NCNT obtained via NH_3 functionalization.[14] However, it was not possible to remove selectively and quantitatively one singular species in order to obtain a pyridine-free sample (HT1300NCNT). Thermal treatment reduced all N species but the thermally most stable N4 species to a lesser extent. We also studied the thermal stability of the N species in situ by temperature-programmed desorption XPS from room temperature up to 700 °C. We found that the thermally desorbed species was mainly the N2 species, while all the others are thermally stable up to 700 °C. This behavior differs from the NCNT obtained via defect-mediated NH_3 functionalization, where in a similar experiment[14] a dynamic interconversion and desorption of the N species was observed with surface retention of mainly the N4 species at temperature of 700 °C. An explanation for this behavior is that the CCVD-growth NCNT presents a carbon structure with a higher graphitic character that host the N species, and this may have implication in the thermal stability of the N species as well their tendency to undergo surface rearrangement. The conversion of the N1 species into N4 is probably hindered by the higher rigidity of the ordered graphitic structure or by the localization of the N1 species in a defective site where the further linkage with a C dangling bond is not accessible.

Structural Characterization of the Pd-Containing Samples. HAADF-STEM image and bright-field HRTEM image of the sample Pd1%NCNT of exactly the same area are shown in Figure S6. The HAADF-STEM shows a NCNT with highly dispersed Pd clusters immobilized on the surface. The highly dispersed Pd clusters are difficult to distinguish from the contrast of the carbon support in HRTEM mode, and only the largest crystalline Pd particles are clearly visible (as for example those in the red cycle). For a comparative analysis of the Pd-based samples, we focus on the qualitative characterization by HAADF-STEM and quantitative CO chemisorption.

Figure 8 compares the HAADF-STEM images for $PdCl_2$NCNT catalysts (a) and the reduced Pd catalysts Pd1%NCNT. A higher dispersion of Pd clusters is observed on the PdCl2-containing samples than on the reduced Pd catalysts. This is always the case for the Pd-complex-containing samples synthesized in this work. The sensitivity of the contrast in HAADF-STEM to atomic number (Z) allows drawing some conclusions about the Pd chemical state.[40]

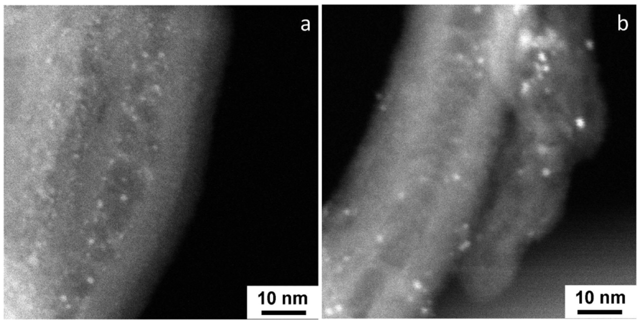

Figure 8. HAADF-STEM image for the sample $PdCl_2$NCNT (a) and Pd1%NCNT (b).

When Pd is atomically dispersed or clustered in a rather disordered arrangement, the contrast is weak and quite diffuse as in the case of the $PdCl_2$-containing samples; for crystalline Pd nanoparticles, the contrast is stronger due to the cubic close-packed manner of the metallic structure. Those particles are also observable by TEM (Figure S6).

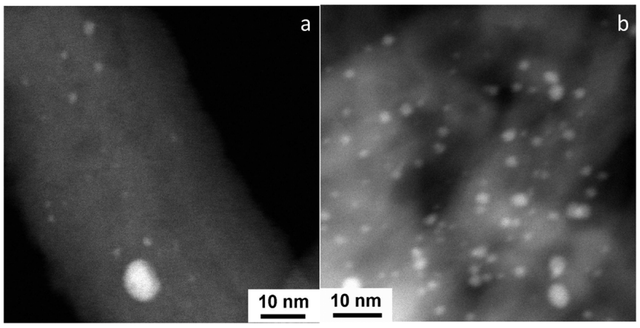

Figure 9. HAADF-STEM image for the sample Pd1%HT1000NCNT (a) and Pd0.3%HT1300NCNT (b).

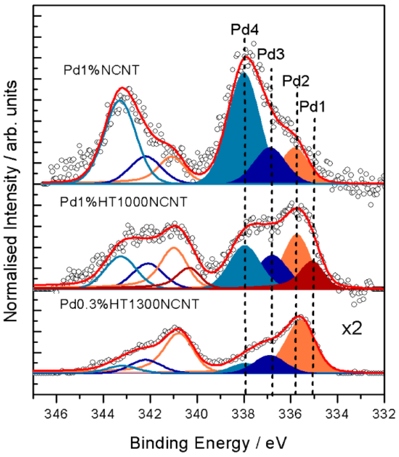

Figure 10. Pd 3d core level spectra at 600 eV KE for the reduced Pd on the different NCNT samples.

Table 2. Relative Abundance (%) of the Components in the Pd 3d Spectra[a]

	component/BE (eV)			
	Pd1	Pd2	Pd3	Pd4
	335	335.5	336.7	337.9
sample	Pd°	Pd°_NP	$Pd\delta^{+}$_NP	Pd^{2+}
Pd1%NCNT	0	26	18	56
Pd1%HT1000NCNT	21	40	17	22
Pd0.3%HT1300NCNT	0	74	17	9

[a] The error in abundance is ca. 20%.

With respect to the Pd1%NCNT (Figure 8b), after the reduction treatment, the average particle size of Pd on the annealed HT1000NCNT and HT1300NCNT (Figure 9) increases more significantly, and the particles are loosely decorating the carbon support. This is also consistently found by CO chemisorption measurements (Table 1). In particular, it was not possible to determine any CO chemisorption on the Pd1%NCNT sample (at the measurements condition used in this study), probably due to the ionic chemical state of the Pd species in this sample. For the Pd1%HT1000NCNT, an average particle size of 5.2 nm is found. This indicates that the removal of the N species by the thermal treatment has reduced considerably the immobilization capacity of the support, leading to an overload of the anchoring sites if the same 1% Pd loading is used as in the case of the NCNTs. However, the average particle size visibly increases also for the Pd on HT1300NCNT (4.2 nm) for which the Pd loading was kept very low (0.3%) with the aim to exclusively immobilize Pd on the N sites. Moreover, the exposed metallic surface area, as determined by CO chemisorption, scales with the Pd loading for the Pd1% HT1000NCNT and Pd0.3%HT1300NCNT and is 0.97 m^2/g and 0.35 m^2/g, respectively (Table 1). This suggests that the Pd chemical state and the resulting particle size are affected also by the nature of the N species and the graphitic structure surrounding the N site. Figure 10 shows the fitted Pd 3d core level spectra for the Pd nanoparticles on the as-received and annealed NCNT sample. The fitting of the Pd 3d was previously described in ref 10, and we briefly recall here the peak assignment. Four components are considered: Pd1 at BE 335 eV; Pd2 with BE in the range 335.55−335.7 eV; Pd3 at 336.9 eV; and Pd4 at 337.8 eV. The relative abundance of those species is summarized in Table 2. The most abundant component for the Pd1%NCNT is the Pd4 component, which was attributed to a divalent Pd species.[10] Consistently, we observe that, regardless the nature of the support, the samples impregnated with the divalent $PdCl_2$ complex present mainly the Pd3 and Pd4 components (see as example Figure 11a for PdCl2NCNT), indicating an analogous electronic configuration of Pd in the Pd1%NCNT (Figure 10). Note that this sample was obtained by a sequential thermal treatment in

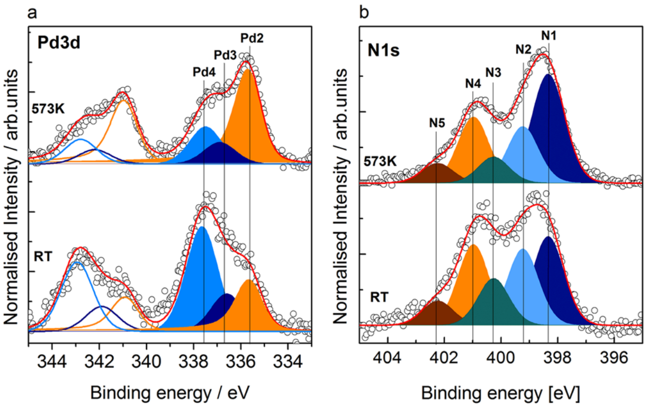

Figure 11. Core level spectra at 600 eV KE for the sample $PdCl_2NCNT$ during in situ reduction (a) Pd 3d and (b) N 1s.

O_2 and H_2 at 200 °C of the $Pd(NO_3)_2$ precursor immobilized on the NCNTs.

Differently, the calcination and subsequent reduction of the $Pd(NO_3)_2$ precursor induce for the Pd1%HT1000NCNT and Pd0.3%HT1300NCNT the relative distribution of Pd species to change with an increase of the amount of Pd2 species in the Pd 3d spectra.

The Pd2 components are indeed attributed to electronically modified metallic Pd nanoparticles by the interaction at the carbon support. Those occur in the HAADF-STEM as nanoparticles of 2−5 nm in diameter. Accordingly to our previous study[10], the Pd3 is possibly located on the surface region of these nanoparticles (Pd2 components) and carries a partial positive charge caused by the intercalation of O or C in and underneath the particle surface.[67] The adsorption of Cl produces in fact also this shift (not shown). The different intensity ratio Pd3/Pd2 found for the different catalysts account for the different geometry of the nanoparticles (Pd2). The Pd1 is assigned to bulk-like metallic palladium. Pd1 species accounts for the very big particles present on the Pd1%HT1000NCNT annealed sample (≅ 10 nm nanoparticle in Figure 9a): those are formed if the Pd precursor weakly interact at the C surface leading to sintering during the calcination and reduction treatment. The divalent Pd species (Pd4) occur on the NCNT as atomically dispersed Pd (see Figure S6b) at the functional groups of the carbon surface or as oxo-hydroxo Pd clusters. Those species are more abundant when Lewis basic sites in the form of pyridine N species are present, which indicates that the coordination at these sites lowers their reducibility at the reduction condition used.

The reduction of the catalyst precursor $PdCl_2NCNT$ was studied in situ by photoemission spectroscopy in UHV up to 300 °C and reported here in Figure 11. Most of the species Pd4 and Pd3, which in this case correspond to the complex precursor (Pd bound to different ligands such as Cl, N, O), undergo a transformation to a Pd2 component assigned to metal nanoparticles upon reduction when approaching 300 °C. The in situ annealing produces also a modification of the N 1s species: the N2 and the N3 components decrease due to the annealing while the N1 components increases such as the N 1s line-shape is now similar to the starting NCNT. The N 1s data show that N−H group (N2 species) decreases, indicating H spillover by the small metallic nanoparticles Pd2 formed under the reductive atmosphere from the metal ionic species Pd4 and Pd3. Additionally the increase of the relative amount of N1 species can be seen as a consequence of the mobility of the Pd nanoparticles during reduction such that some of the underlying N1 species at which the Pd3 and Pd4 were coordinated can become surface exposed. Interestingly, on the HAADF-STEM investigation of Pd0.3%HT1300NCNT (Figure 9b), extreme particle overgrowth (Pd1) was not observed, and in fact, the Pd2 component is the most abundant species in the Pd 3d spectrum (Figure 10). Considering that this support is characterized by substitutional N in 3-fold coordination, described in Figure 1, one can assume that the stabilization of Pd2 components occur at these sites. In principle, hydrogenation of the carbon support through activated hydrogen from the Pd particles preferentially attacks the N4 sites due to the charge localization. In this way, the Pd mobilizes itself gradually, and particle growth is the consequence. Only those Pd species that are unable to activate hydrogen by hydride formation[68−70] are safe against this self-destruction of the anchoring sites. Small particles with a shifted d-band due to strain or stable modification by subsurface compound[71−74] formation are the long-term stable species.

Study of the N−Pd Interaction by N 1s NEXAFS. Extra-molecular interactions involving the N site can be evaluated by NEXAFS spectroscopy. Stöhr[65] has described the C 1s core excitation of unsaturated organic molecule chemisorbed on a metal surface. The bonding of unsaturated molecule and a transition metal involves a σ bond formation from the donation of a filled π bonding molecular orbital from the molecule to the empty $d\sigma$ orbital of the metal and the π back-donation from filled $d\pi$ orbital of the metal to the empty π^* antibonding MO of the molecule. This treatment can be extended to the case of NCNTs considered as macromolecule with localized functional groups[5] acting as chemisorption sites for metal. In this case, the σ carbon−metal bonds involve a lone pair (Lewis base donors) and a π hybridized orbital of the support with electron transfer from the support to the metal. The extra-molecular interactions can range from weak to comparable to intramolecular bond strength. This produces modifications in the intensity as well as the width of the NEXAFS resonances. In Figure S7, the N 1s core excitation spectrum of blank NCNT support is compared to those of the carbon support after Pd immobilization. The blank NCNT was prepared to better evaluate the participation of Pd in interactions with the N functional groups and exclude the participation of other atoms (Blue curve in Figure S7). As consequence of the Pd immobilization, we observe a reduction of the intensity of the resonance R1 assigned to pyridine-like N species. This intensity drop upon complex formation indicates a reduction of unoccupied states in the pyridine orbitals. That is, a metal−support π back-bonding interaction affects the N $1\sigma-\pi^*$ transition. Thus, the lone pair orbital of the pyridine-like N forms a σ donor stabilized by back-bonding of metal $d\pi$-$p\pi$ orbitals with the N π^* antibonding orbitals. The increase of the bond strength will increase the metal $d\pi$-$p\pi$ contribution to the π^* orbital, and as consequence, the π^* resonance intensity will decrease. A close inspection reveals a shoulder to the lower photon energy side (Figure 12) of the π^* resonance for all the Pd-containing samples. This can be interpreted in two different ways: increase of the resonance broadening or shift of the resonance position. Both interpretations indicate charge localization on the N atom and a charge transfer between donor/acceptor sites upon complex formation.

Metal valence electrons may mix with the π^* states of the N atom in the carbon support if a strong bonding results between support and Pd. Therefore, the excited electron at the nitrogen

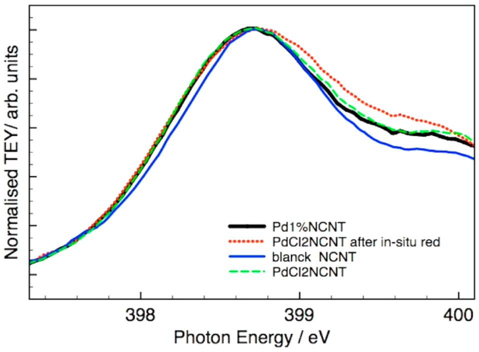

Figure 12. Experimental TEY N 1s core excitation NEXAFS spectra in the R1 resonance for NCNT-based samples (normalization to the R1 resonance at 398.8 eV).

can decay into the metal conduction band, and the reduced lifetime of the excited state leads to broadening of the resonance. This implies a final state relaxation process typical of bond configurations of charged systems.

In contrast to XPS, the π^* resonance position in NEXAFS is rather insensitive to extra-molecular interaction, and the transition energy is not affected by the relaxation shift from extra-molecular interaction. The reason being that the atom remains neutral in the excitation process and the core-hole is shielded by the excited electron in the π^* orbital. If the shoulder seen in the Pd-containing samples is due to a shift of the 1s-π^* resonance, initial state effects are involved that shift the position of the N 1s core level. This would be caused by a variation of the charge localized on the N atoms. The direction of the shift is indicative of the charge localized on the N: more negative charge produces a shift to lower energy.[75] This agrees with the shift of the Pt L edge to higher photon energy reported in literature for Pt nanoparticles on graphene oxide.[40]

The in situ reduced sample (red spectrum) shows a more pronounced broadening of the R1 resonance that can be interpreted also as a shift of the R1 π^* resonance to the higher energy side. This treatment produces the in situ formation of the Pd2 component (Figure 11). Accordingly, the interaction between the N-pyridine species and the Pd2 species (Pd nanoparticle) also occurs inducing charge depletion on the N atoms. This change of the charge transfer direction is expected during the catalytic reaction boosted by the reactive atmosphere and it explains observed dynamics in reactivity.

The σ^* resonance remains in the same position; the reason is that the final state is sufficiently localized to be self-screened. This implies that also the bond distance is not modified.

The impact of the Pd coordination at the 3-fold coordinated N was evaluated by analyzing the variation of the R3 resonance of the N 1s core excitation NEXAFS spectra for the HT1300NCNT samples series reported in Figure 13. These samples were chosen as they are mainly containing the species responsible for the R3 resonance. It can be observed that the intensity of the R3 resonance decreases for the Pd-containing samples. This is the case for the PdCl$_2$HT1300NCNT, for the Pd1%HT1300NCNT and for the Pd0.3%HT1300NCNT. Especially, the reduced samples show overlapping spectra. The HClHT1300NCNT shows only partial reduction of the R3 intensity if compared to the Pd samples. However, differently from the R1 resonance, the R3 resonance maintains similar broadening.

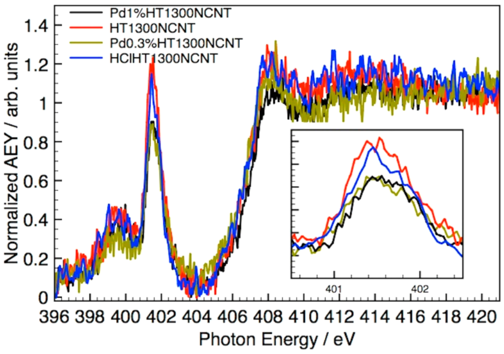

Figure 13. Experimental N 1s core excitation NEXAFS spectra for HT1300NCNT-based samples; detail of the R3 resonance at 401.4 eV (inset). The spectra were recorded in the Auger yield detection mode (AEY) and normalized to the edge jump.

Therefore, a covalent bond between the hybridized π orbitals of the N atoms and the dπ-pπ orbitals of the Pd atom occurs without perturbation of the charge density. The decrease of the R3 intensity, more pronounced for the reduced sample is due to a change in hybridization of the π^* states which assume more σ character. The sketch reported in Figure 14 clarifies the bonding situation resembling the so-called Blyholder moldel.[76] In summary, upon impregnation at acid pH, the electrostatic interaction between the positively charged (protonated) N species and the metal complexes in solution (probably [Pd$_x$(NO3)$_{2x+1}$]$^-$ complexes[77]) occurs first. If the loading is kept low enough (1 wt %/wt of Pd vs N 5 wt %/wt as determined by EDX in the case of the Pd1%NCNT) single metal coordination at the N site may prevail on the condensation of the Pd complexes. Upon reduction at 200 °C, the metal oxide species formed in the previous oxidation step might undergoes reduction and clustering. This occurs through hydrogenation of the chemical bond of Pd at the anchoring sites, which mobilize the Pd atoms toward the formation of bigger particles. We found that the pyridine-like species on the NCNT (Pd1%NCNT sample) is mainly involved in the immobilization of ionic atomically dispersed Pd and nanoclusters of oxo-hydroxo species (Pd4).

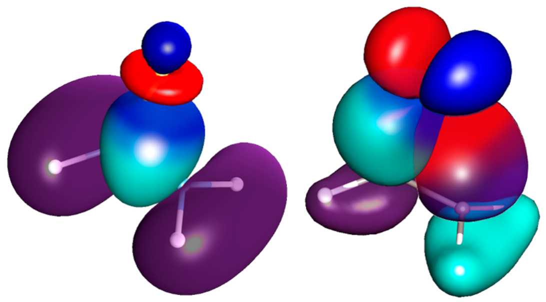

Figure 14. σ-bond between an empty metal d-orbital (negative lobe in blue and positive lobe in red) and a filled π-orbital (negative lobe in pale blue and positive lobe in purple) from the support (on the left); π-backbond between filled metal d-orbital and empty π^*-antibonding orbital of the support (on the right).

If the loading of the metal precursor is higher than a threshold value dictated by the population of N species, see case of annealed NCNT, we observe an increase of the Pd nanoparticles component Pd2 as well as the bulk-like Pd component, Pd1. In the case of HT1300NCNT, though the

Table 3. Catalytic Results for Selective Hydrogenation of Phenyl Acetylene to Styrene[a]

	Pd1%NCNT	Pd1%HT1000NCNT	Pd0.3%HT1300NCNT
initial activity $[\text{mol}_{\text{Sty}}]/(\text{h*gPd})]$	5.1	173.9	65.9
initial activity $[\text{mol}_{\text{Sty}}]/(\text{h*m}^2)]$[a]	n.d.	1.8	0. 6
S_{Sty} (X_{PhenAc}~10%) [%]	91.5	95.5	95.5
S_{Sty} ($X_{\text{PhenAc}} \geq 99\%$) [%]	n.d.	87.0	74.0

[a] Pd Surface area determined by CO chemisorption.

loading was kept very low (0.3%), we observe the formation of mainly the Pd2 component related to metallic Pd nanoparticles electronically modified by the interaction at the C surface. We found that the 3-fold substitutional N is involved in covalent bond with the Pd, and we concluded that those are the small metallic Pd nanoparticles electronically modified by the interaction with the support (Pd2). We consider this situation as of particular relevance for sustained catalytic action and recall that the combination of microscopy and spectroscopy has provided us with a lead structure for future optimization of the notoriously unstable Pd-carbon catalyst family.

Catalytic Performance of NCNT-Based Samples. We expect that the modulation of the metal−support interactions has a relevant effect on the resulting catalytic activity, and thus, we evaluate the catalytic behavior of Pd nanoparticles immobilized on NCNT containing different N species. We study the behavior of these catalysts for hydrogenation and oxidation reaction. In particular, the reactions of interest are the liquid-phase selective hydrogenation of phenyl acetylene to styrene, the CO oxidation, and ORR in alkaline media.

Hydrogenation of Phenyl Acetylene. The catalytic properties of transition metals like Pd strongly depend on its electronic structure,[73] which modifies the adsorption strength of alkynes and alkenes. In the present batch experiments, phenyl acetylene is primarily hydrogenated to styrene, and the tested catalysts (Table 3) show a relatively high selectivity of >90% at low conversions of phenyl acetylene. The undesired side-reaction, the hydrogenation of styrene to ethyl-benzene, becomes dominant at high or full conversion. The high selectivities to the alkene of Pd catalysts (i.e., a suppressed ethyl benzene formation) are achieved due to the presence of a subsurface Pd−C phase, which is formed by an initial rapid dehydrogenation of alkynes and diffusion of C into Pd.[39,72,78] The observed sudden decrease of phenyl acetylene consumption and styrene formation at the beginning of the reaction (for Pd1%HT1000NCNT see Figure S8) is accompanied by a sudden decrease in the carbon balance, indicating the formation of subsurface Pd−C and carbonaceous deposits. The Pd−C phase decomposes if the chemical potential of the alkyne is too low compared to the potential of hydrogen,[78] and, hence, the tested catalysts lose their selectivity at high conversion, which is often observed with metallic Pd catalysts.[79,80] Interestingly, the Pd1%NCNT sample is much less active than the Pd1%HT1000NCNT and the Pd0.3%HT1300NCNT catalysts. The Pd3 and Pd4 species are apparently rather inactive for alkyne hydrogenation. Pd4, representing a strongly N-bound Pd^{2+} species, was shown to be unable to significantly activate hydrogen for self-hydrogenation. In this way, it can be seen that stable Pd nanoparticles that do not self-hydrogenate the carbon support are also poorly active in hydrogenation of even a highly activated C−C triple bond.

The ~3 times higher activity of Pd1%HT1000NCNT compared to Pd0.3%HT1300NCNT can be explained by the higher amount of Pd1 (bulk-like Pd nanoparticles) with respect to Pd2 (electronically modified Pd nanoparticles by the interaction at the carbon surface) in this material (Table 2). These results support the observations in ref 81 that a strong electronic modification of Pd indeed significantly lowers the activity but does not increase selectivity. High selectivity to alkenes is hardly achieved at high alkyne conversions by solely electronic modification via carbon metal support interaction but are rather obtained by a well-directed site-blocking of unselective sites (e.g., with heavy metals like in the case for Lindlar's catalyst).[82] For the selective hydrogenation of alkynes, the concept of N stabilization of unprotected nanoparticles obtained via impregnation seems to be inadequate at the mild hydrogenation condition used.

CO Oxidation. The catalytic activity of the Pd samples in the CO oxidation at atmospheric pressure is reported in Figure 15. Without any pretreatments, the samples were exposed to a $CO/O_2/He$ mixture (2:1:97), and repetitive heating/cooling cycles were performed. In general, the heating cycles in Figure 15 follow conversion versus temperature profiles that are

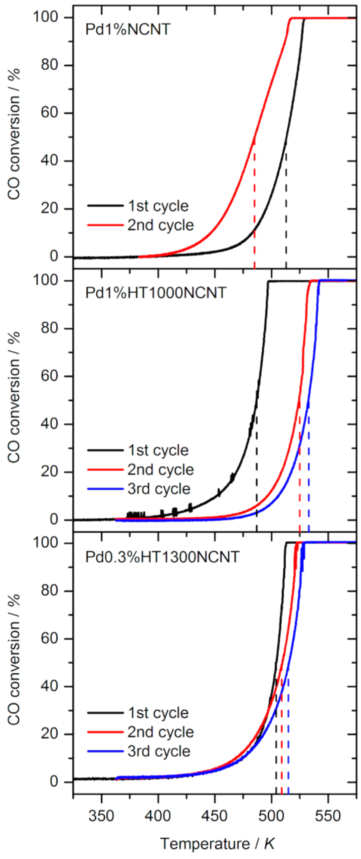

Figure 15. Light-off measurement of CO oxidation. Vertical dashed lines represent the respective T_{50} temperatures.

expected for a Langmuir−Hinshelwood-mechanism, which is well-known to occur on Pd in CO oxidation.[83,84] Pd1%NCNT shows surprising behavior, because in the second heating cycle, a much higher CO conversion is observed compared to the first heating cycle. Looking at the Pd 3d spectrum in Figure 10 (top), this phenomenon can be explained by reduction of the majority of Pd^{2+} species (Pd4) in the CO-containing feed. Thus, the second heating cycle shows higher conversion because more reduced Pd species are now present. These results clearly are in line with the results obtained in the semihydrogenation of phenyl acetylene (cf. Table 3), which also showed very low initial activity on Pd1%NCNT. The reduction of Pd1%NCNT during the first heating cycle becomes even more rational when comparing the second cycle to the first cycle of Pd1%HT1000NCNT, because they are very similar, showing both a T50 temperature (= temperature at 50% conversion) of around 485 K. Pd1%HT1000NCNT showed a much higher ratio of reduced Pd species in XPS, hence it can be concluded that the Pd state present on Pd1%NCNT is approaching in the second CO oxidation cycle the state of Pd1%HT1000NCNT. However, Pd1%HT1000NCNT is apparently not very stable in this reaction, as indicated by the strong deactivation with increasing cycle number. Reasons for deactivation can be manifold: we suppose sintering to be one of the main reasons. With respect to the level of accuracy of the analyzer, all formed CO_2 originates from CO, and therefore, no significant burning of the NCNTs takes place. The conversion of Pd0.3%HT1300NCNT in the first cycle is lower compared to Pd1%HT1000NCNT. This can be simply explained by the lower Pd loading and lower exposed metallic surface area, considering that the same amount of catalyst was used for each sample. Nevertheless, Pd0.3%HT1300NCNT shows only slight deactivation, which is indicated by the T_{50} temperatures that increased by only ca. 5 K with increasing heating cycle number. A reason for the better stability is the strong interaction of the Pd2 nanoparticles at the N sites in Pd0.3%HT1300NCNT. The reactivity is indeed correlated to the electronic state of the Pd induced by the support. On Pt(110) in CO oxidation, Ertl[85] found that the oxygen coverage is proportional to a change of the work function, which is directly related to an increase in CO_2 formation. Hence, here one could suspect that the strong deactivation processes in Pd1%HT1000NCNT is related to diffusion of oxygen into the subsurface, which lowers the work function and thus the CO_2 formation; this process is probably reduced for the electronically modified Pd2 species of the Pd0.3%HT1300NCNT, which are surface saturated by O impurities (Pd3 in Figure 10).

ORR. Cyclic voltammetry (CV) was used to study the electrochemical behavior of the NCNT samples and the Pd supported on NCNT samples in N_2-saturated solution and O_2-saturated solutions (Figure S9a,b). Owing to the very low metal loading, under N_2-saturated solution, the CV profiles for all the samples are dominated by the capacitance behavior of the C support. We observe that the annealing of the NCNTs reduces the capacitance, and in contrary, the addition of the Pd to the NCNT enhances the capacitance. This is not the case for the Pd0.3%HT1300NCNT, which show similar trend as the bare support indicating higher hydrophobic character. Under O_2-saturated solution, ORR is observed in the CV of Figure S9b and in the rotating disk linear voltammetry (LV) of Figure 16. The ORR for all NCNTs is under diffusion control for potentials below 0.65 V, but is under kinetic control for the potential region between 0.65 and 0.8 V. The ORR onset potential and half-wave potentials are summarized in Table4. The metal-free NCNT shows quite interesting catalytic activity for ORR with an onset potential at 0.86 V and a half wave potential of 0.69 V. The onset potential is slightly lower than the value reported for NCNT by Zhao et al.[6] The current density in the kinetically controlled region is an important kinetic parameter representing the electrochemical reaction rate. At a given potential, higher current density implies higher catalytic activity. Additionally, it is also desirable to have the onset potential of oxygen reduction as close as possible to the reversible electrode potential (thermodynamic electrode potential). A shift from this value represents the overpotential. Because the NCNT is active for ORR, initially we took particular care to evaluate the influence of the impurities on the electrocatalytic performance. For this reason, not-cleaned carbon supports were compared with the purified ones (Figure S10). As we could not observe significant changes in the electrochemical behavior after cleaning, the systematic analysis of the catalytic performance focuses on the not-cleaned support used throughout the rest of this study. The annealing treatment at 1300 °C of the NCNT (HT1300NCNT sample) affects the catalytic performance in the ORR. In particular, the onset potential shifts 20 mV to lower value but the limiting current density increases substantially to 5.2 mA/cm^2. Therefore, the thermal desorption of most of the N species in pyridine-like structure does not compromise the activity of the NCNT for ORR. This suggests that the most thermally stable N species plays the dominant role in the electrocatalytic properties. Liu et al.[86] studied the ORR in alkaline media for nitrogen-doped ordered mesoporous graphitic array and showed that by increasing the temperature of pyrolysis of the organic precursor, the onset potential as well as the current density increased substantially.

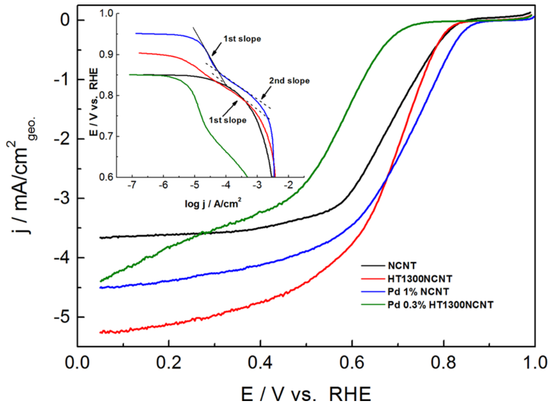

Figure 16. Linear sweep voltammogram in O_2-saturated KOH 0.1 M (scan rate 10 mV/s and 1600 rpm); Tafel plot relative to the kinetically controlled region (inset). The 1st slope is at the highest potential region and 2nd slope is at lower potential region.

These results are in agreement with the work of Lai et al.[87], in which graphitic N species formed at higher temperature played the most important role in ORR activity. This is also in agreement with the enhancement of oxidation catalytic activity of N-doped active carbons observed much earlier.[12,60]

The immobilization of 1 wt % of Pd on the NCNT (Pd1%NCNT) leads to shift of the onset potential to 0.88 V and a half-wave potential of 0.78 V. The enhancement of the ORR may be attributed to the presence of Pd subnanometer clusters coordinated at the N sites. The Pd nanoclusters can act as

Table 4. Summary of Electrochemical Parameters

sample	onset ORR/V	HWP/V	Tafel mV/dec		n e$^-$	
			first	second	0.5 V	0.3 V
NCNT	0.86	0.69	95		3.6	4.0
HT1300NCNT	0.84	0.71	91		4.0	4.0
Pd1%NCNT	0.88	0.78	149	51	2.8	2.7
Pd0.3%HT1300NCNT	0.75	0.58	196	89	2.7	2.8

Table 5. Summary of Pd−N Species and Reactivity

species	bulk-Pd°	Pd°_NP	Pdδ^+_NP	Pd2$^+$
Pd components	Pd1	Pd2	Pd3	Pd4
interaction sites	C	N4	N4	N1
nanoparticles size	>10 nm	2−5 nm	surface site 2−5 nm	atomically Pd
hydrogenation reactivity	high	low	no	no
CO oxidation reactivity	high	low	very low	very low
ORR	very low	very low	-	active

electron transfer mediator or by increasing adsorption sites for O_2. Differently the immobilization of 0.3% Pd on the annealed NCNT (Pd0.3%HT1300NCNT) is detrimental for the catalytic activity. In fact the onset potential of ORR shifts to lower potential value (0.75 V), indicating an increase of the ORR overpotential.

The Tafel plots relative to the LV data in the kinetically controlled region are shown in the inset in Figure 16, and values are summarized in Table4. The presence of two slopes for the Pd nanoparticles samples indicates that Pd introduces an additional reaction pathway for ORR in addition to the reaction path occurring on the NCNT. The single Tafel slopes occurs for the NCNT and HT1300NCNT at high potential (kinetically controlled region) and has a similar value of about 90 mV/dec.

In the case of Pd-containing samples the first slope has a value of 149 mV/dec for Pd1%NCNT and 196 mV/dec for Pd0.3%HT1300NCNT. The initial high value of the Tafel slope indicates a very slow process.

An additional slope can be considered for the Pd-containing samples occurring at lower potential which has a value of 51 mV/dec for Pd1%NCNT, and a value of 89 mV/dec for the Pd0.3%HT1300NCNT: the decrease of the Tafel slope indicates an acceleration of the reaction which is especially fast for the Pd1%NCNT. The Koutchy−Levich (KL) plots not corrected for the non-ORR current,[88] in Figure S11,S12, allow determining approximately the number of electrons transferred during the reaction.

The calculated values are also summarized in Table 4. It can be seen that, while for both N-containing carbon nanotubes the number of electrons approach a value of 4, which means a dominant 4 e$^-$ transfer, the Pd-containing samples are characterized by a value of 2.7. This means that the mechanism for ORR changes by the addition of Pd to a dominant 2 e$^-$ transfer mechanism leading to a prevalent H_2O_2 formation. We can therefore conclude that the highly thermally stable N species in the N-containing CNT gives rise to the 4 e$^-$ mechanism of O_2 reduction to H_2O. Moreover, the N in pyridine species contributes mainly to the capacitance behavior as well as coordination center for Pd. The addition of Pd on the HT1300NCNT is detrimental for the ORR kinetic due to the blocking effect of the coordinated Pd nanoparticles on the highly thermally stable N species.

Similarly the dominant reaction mechanism for the Pd1% NCNT occurs on the oxo-hydroxo Pd nanoclusters leading to H_2O_2 formation; however, in this case, we can observe that the ORR onset was shifted to higher potential with respect to the NCNT, and this contribution to the overall catalytic performance is actually characterized by an increased kinetic of ORR as shown by the low Tafel slope. With other transition metals such as Fe, a much better catalyst would have resulted, as the peroxide formation would probably be unsupported.

■ CONCLUSION

In this study, we have systematically investigated the nature of the N species in NCNT synthesized by CCVD. By a combined theoretical and experimental XPS and NEXAFS study of the N 1s core excitation, we provide a description of the high thermally stable graphitic N, which is a 3-fold substitutional N species. We have shown that the simple chemical system C−N−Pd gave rise to a multitude of species with different chemical assignments. We have clarified the nature of the interactions of the N species on NCNTs with a metal center such as Pd immobilized via impregnation and their implications in three examples of catalytic reactions. Those results are summarized in Table 5. Upon impregnation and sequential thermal treatment at 200 °C in O_2 and in H_2, atomically dispersed and clustered divalent Pd interacts through a partial ionic character with the pyridinic N functional groups on the NCNTS surface. For highly thermally treated NCNT (HT1300NCNT), the wet impregnation of Pd leads to the formation of metallic Pd nanoparticles electronically modified by the interaction at the C surface. The results presented here suggest that those species are stabilized covalently at the most thermally stable 3-fold substitutional N.

The reported catalytic activity in CO oxidation in the hydrogenation of phenyl acetylene and ORR allows drawing some conclusions about the impact on the reactivity of the Pd/NCNT system. Interestingly, in the CO oxidation, it was possible to identify the graphitic N species as a more stable hosting site for electronically modified Pd nanoparticles responsible for the enhanced catalytic performance in oxidation catalysis. For the hydrogenation reaction, high hydrogenation ability is also required, for which the selectivity can be tuned by site-blocking strategies. This indicates that for each application the electronic structure of the active species need to be tailored according to the concept of structure sensitivity. In the ORR, although small, the reactivity variation among the samples investigated is of considerable importance because it shows that, with the appropriate preparation, it is possible to devise a very active electrocatalyst for ORR. Based on our results, an optimal ORR catalyst should contain an active metal for ORR species as subnanometer metal clusters coordinated at the pyridinic N species together with the metal-free most thermally stable N species. The present work has shown that both the modification of the support and the method of metal addition are critical parameters that in combination can give a multitude of species in the seemingly simple system. The use of a structurally well-defined form of reactive carbon has allowed these insights with experimental and theoretical methods that are hard to apply with the ill-defined but much more popular supports of defective forms of active carbon. The results presented here should allow modifying active carbon in a rational way using descriptors and may motivate the use of today available CNT supports. N-functionalization of nanocarbon offers this possibility.

■ ASSOCIATED CONTENT

Ⓢ Supporting Information

The following file is available free of charge on the ACS Publications website at DOI: 10.1021/acscatal.5b00094.

> Experimental conditions for material properties characterization and additional results data (PDF)

■ AUTHOR INFORMATION

Corresponding Author

*E-mail: arrigo@fhi-berlin.mpg.de.

Notes

The authors declare no competing financial interest.

■ ACKNOWLEDGMENTS

Nobert Pfänder and Gisela Weinberg are acknowledged for the electron microscopy investigations reported in Figure S1 and S2, respectively. HZB (Bessy II) is acknowledged for support during beamtime. The authors thank the BMBF (FKZ03X0040H) and the CarboScale project for funding. G.W. acknowledges support from Uop.

■ REFERENCES

(1) Terrones, H.; Lv, R.; Terrones, M.; Dresselhaus, M. S. *Rep. Prog. Phys.* **2012**, *75*, 062501(30).

(2) Figureido, J. L.; Pereira, M. F. R. In *Carbon Materials in Catalysis*; Serp, P., Figureido, J. L., Eds.; John Wiley & Sons: Hoboken, NJ, 2009; pp 177−208.

(3) Frank, B.; Blume, R.; Rinaldi, A.; Trunschke, A.; Schlogl, R. *Angew. Chem., Int. Ed.* **2011**, *50*, 10226−10230.

(4) Su, D. S.; Perathoner, S.; Centi, S. *Catal. Today* **2012**, *186*, 1−6.

(5) Medjanik, K.; Chercka, D.; Nagel, P.; Merz, M.; Schuppler, S.; Baumgarten, M.; Muellen, K.; Nepijko, S. A.; Elmers, H.-J.; Schoenhense, G.; Jeschke, H. O.; Valenti, R. *J. Am. Chem. Soc.* **2012**, *134*, 4694−4699.

(6) Zhao, A.; Masa, J.; Schuhmann, W.; Xia, W. *J. Phys. Chem. C* **2013**, *117*, 24283−24291.

(7) Shin, D.; Jeong, B.; Mun, B. S.; Jeon, H.; Shin, H.-J.; Baik, J.; Lee, J. *J. Phys. Chem. C* **2013**, *117*, 11619−11624.

(8) Arrigo, R.; Schuster, M. E.; Wrabetz, S.; Girgsdies, F.; Tessonnier, J. P.; Centi, G.; Perathoner, S.; Su, D. S.; Schlogl, R. *ChemSusChem* **2012**, *5*, 577−586.

(9) Arrigo, R.; Wrabetz, S.; Schuster, M. E.; Wang, D.; Villa, A.; Rosenthal, D.; Girsgdies, F.; Weinberg, G.; Prati, L.; Schlogl, R.; Su, D. S. *Phys. Chem. Chem. Phys.* **2012**, *14*, 10523−10532.

(10) Arrigo, R.; Schuster, M. E.; Abate, S.; Wrabetz, W.; Amakawa, K.; Teschner, D.; Freni, M.; Centi, G.; Perathoner, S.; Havecker, M.; Schlogl, R. *ChemSusChem* **2014**, *7*, 179−194.

(11) Boehm, H. P.; Mair, G.; Stoehr, T.; de Rincbn, A. R.; Tereczki, B. *Fuel* **1984**, *63*, 1061−1063.

(12) Stöhr, B.; Boehm, H. P.; Schlögl, R. *Carbon* **1991**, *29*, 707−720.

(13) Arrigo, R. *N-functionalization of CNFs and application in heterogeneous catalysis*. Ph.D. Thesis, Technische Universität Berlin, Berlin, 2009.

(14) Arrigo, R.; Havecker, M.; Schlogl, R.; Su, D. S. *Chem. Commun.* **2008**, 4891−4893.

(15) Kutzelnigg, W.; Fleischer, U.; Schindler, M. *NMR Basic Principles and Progress*; Springer: Berlin, NY, 1990.

(16) Buckley, A. N. *Fuel Process. Technol.* **1994**, *38*, 165−179.

(17) Liu, R.; Wu, D.; Feng, X.; Muellen, K. *Angew. Chem., Int. Ed.* **2010**, *49*, 2565−2569.

(18) dos Santos, M. C.; Alvarez, F. *Phys. Rev. B: Condens. Matter Mater. Phys.* **1998**, *58*, 13918−13924.

(19) Miyamoto, Y.; Cohen, M. L.; Louie, S. G. *Solid State Commun.* **1997**, *102*, 605−608.

(20) Marton, D.; Boyd, K.; Al-Bayati, A.; Todorov, S.; Rabalais, J. *Phys. Rev. Lett.* **1994**, *73*, 118−121.

(21) Liu, A.; Wentzcovitch, R. *Phys. Rev. B: Condens. Matter Mater. Phys.* **1994**, *50*, 10362−10365.

(22) Thomas, A.; Fischer, A.; Goettmann, F.; Antonietti, M.; Muller, J. O.; Schloegl, R.; Carlsson, J. M. *J. Mater. Chem.* **2008**, *18*, 4893−4908.

(23) Czerw, M. T. R.; Charlier, J.-C.; Blase, X.; Foley, B.; Kamalakaran, N. G. R.; Terrones, H.; Tekleab, D.; Ajayan, P. M.; Blau, W.; Carroll, M. R.; Carroll, D. L. *Nano Lett.* **2001**, *1*, 457−460.

(24) Robertson, J.; Davis, C. A. *Diamond Relat. Mater.* **1995**, *4*, 441−444.

(25) Kondo, T.; Casolo, S.; Suzuki, T.; Shikano, T.; Sakurai, M.; Harada, Y.; Saito, M.; Oshima, M.; Trioni, M. I.; Tantardini, G. F.; Nakamura, J. *Phys. Rev. B: Condens. Matter Mater. Phys.* **2012**, *86*, 0354361−0354366.

(26) Gong, F. D. K.; Xia, Z.; Durstock, M.; Dai, L. *Science* **2009**, *323*, 760−764.

(27) Britto, P. J.; Santhanam, K. S. V.; Rubio, A.; Alonso, J. A.; Ajayan, P. M. *Adv. Mater.* **1999**, *11*, 154−157.

(28) Yang, L.; Jiang, S.; Zhao, Y.; Zhu, L.; Chen, S.; Wang, X.; Wu, Q.; Ma, J.; Ma, Y.; Hu, Z. *Angew. Chem., Int. Ed.* **2011**, *50*, 7132−7135.

(29) Owens, F. J. *Mater. Lett.* **2007**, *61*, 1997−1999.

(30) Khavryuchenko, O.; Frank, B.; Trunschke, A.; Hermann, K.; Schlögl, R. *J. Phys. Chem. C* **2013**, *117*, 6225−6234.

(31) Zhang, L.; Xia, Z. J. *J. Phys. Chem. C* **2011**, *115*, 11170−11176.

(32) Costentin, C.; Drouet, S.; Robert, M.; Saveant, J. M. *Science* **2012**, *338*, 90−94.

(33) Vitale, V.; Curioni, A.; Andreoni, W. *J. Am. Chem. Soc.* **2008**, *130*, 5848−5849.

(34) Adjizian, J. J.; De Marco, P.; Suarez-Martinez, I.; El Mel, A. A.; Snyders, R.; Gengler, R. Y. N.; Rudolf, P.; Ke, X.; Van Tendeloo, G.; Bittencourt, C.; Ewels, C. P. *Chem. Phys. Lett.* **2013**, *571*, 44−48.

(35) Suarez-Martinez, I.; Felten, A.; Pireaux, J. J.; Bittencourt, C.; Ewels, C. P. *J. Nanosci. Nanotechnol.* **2009**, *9*, 6171−6175.

(36) Lin, S. D.; Hsu, Y.-H.; Jen, P.-H.; Lee, J.-F. *J. Mol. Catal. A: Chem.* **2005**, *238*, 88−95.

(37) Zhou, J. G.; Williams, Q. L. *J. Nano Res.* **2011**, *15*, 29−40.

(38) Abel, E. W.; Stone, F. G. A.; Puddephatt, R. J.; Wilkinson, G. In *Comprehensive Organometallic Chemistry II: Nickel, Palladium, Platinum*; Puddephatt, R. J., Ed.; Pergamon Press: Oxford, U.K., 1995; Vol. 9.

(39) Teschner, D.; Vass, E.; Havecker, M.; Zafeiratos, S.; Schnorch, P.; Sauer, H.; Knop-Gericke, A.; Schlogl, R.; Chamam, M.; Wootsch, A. *J. Catal.* **2006**, *242*, 26−37.

(40) Sun, S.; Zhang, G.; Gauquelin, N.; Chen, N.; Zhou, J.; Yang, S.; Chen, W.; Meng, X.; Geng, D.; Banis, M. N.; Li, R.; Ye, S.; Knights, S.; Botton, G. A.; Sham, T. K.; Sun, X. *Sci. Rep.* **2013**, *3*, 1775.

(41) Wolf, A.; Michele, V.; Mleczko, L.; Assmann, J.; Buchholz, S. Patent No. WO2009/080204.

(42) Buchholz, S.; Duff, D. G.; Michele, V.; Mleczko, L.; Muennich, C.; Rudolf, R.; Wolf, A. Patent No. WO2006/050903..

(43) Tessonnier, J.-P.; Becker, M.; Xia, W.; Girgsdies, F.; Blume, R.; Yao, L.; Su, D. S.; Muhler, M.; Schlögl, R. *ChemCatChem* **2010**, *2*, 1559−1561.

(44) Becker, M. J.; Xia, W.; Tessonnier, J.-P.; Blume, R.; Yao, L.; Schlögl, R.; Muehler, M. *Carbon* **2011**, *49* (15), 5253−5264.

(45) Tougaard, S. *J. Vac. Sci. Technol., A* **1996**, 1415−1423.

(46) Hermann, K.; Petterson, L. G. M. *StoBe Software*, version 3.1; deMon developers group: Montreal, Canada, 2011; see http://www.fhi-berlin.mpg.de/KHsoftware/StoBe/.

(47) Cavalleri, M.; Hermann, K.; Knop-Gericke, A.; Hävecker, M.; Herbert, R.; Hess, C.; Oestereich, A.; Döbler, J.; Schlögl, R. *J. Catal.* **2009**, *262*, 215−223.

(48) Hammer, B.; Hansen, L. B.; Nørskov, J. K. *Phys. Rev. B: Condens. Matter Mater. Phys.* **1999**, *59*, 7413−7421.

(49) Perdew, J. P.; Burke, K.; Ernzerhof, M. *Phys. Rev. Lett.* **1996**, *77*, 3865−3868.

(50) Triguero, L.; Petterson, L. G. M.; Ågren, H. *Phys. Rev. B: Condens. Matter Mater. Phys.* **1998**, *58*, 8097−8110.

(51) Ågren, H.; Caravetta, V.; Vahtras, O.; Pettersson, L. G. M. *Chem. Phys. Lett.* **1994**, *222*, 75−81.

(52) Leetmaa, M.; Ljungberg, M. P.; Lyubartsev, A.; Nilsson, A.; Pettersson, L. G. M. *J. Electron Spectrosc. Relat. Phenom.* **2010**, *177*, 135−157.

(53) Kolczewski, C.; Püttner, R.; Plashkevych, O.; Ågren, H.; Staemmler, V.; Martins, M.; Snell, G.; Schlachter, A. S.; Sant'Anna, M.; Kaindl, G.; et al. *J. Chem. Phys.* **2001**, *115*, 6426−6437.

(54) Kolczewski, C.; Hermann, K. *Surf. Sci.* **2004**, *552*, 98−110.

(55) Schuster, M. E. *Structure and Reactivity of Diesel Soot Particles from Advanced Motor Technologies*. Ph.D. Thesis, Technische Universität Berlin, Berlin, 2011.

(56) Schuster, M. E.; Haevecker, M.; Arrigo, R.; Blume, R.; Knauer, M.; Ivleva, N. P.; Su, D. S.; Niessner, R.; Schlogl, R. *J. Phys. Chem. A* **2011**, *115*, 2568−2580.

(57) Abbas, G.; Papakonstantinou, P.; Iyer, G.; Kirkman, I.; Chen, L. *Phys. Rev. B: Condens. Matter Mater. Phys.* **2007**, *75*, 195429−195438.

(58) Schiros, T.; Nordlund, D.; Pálová, L.; Prezzi, D.; Zhao, L.; Kim, K. S.; Wurstbauer, U.; Gutiérrez, C.; Delongchamp, D.; Jaye, C.; Fischer, D.; Ogasawara, H.; Pettersson, L. G. M.; Reichman, D. R.; Kim, P.; Hybertsen, M. S.; Pasupathy, A. N. *Nano Lett.* **2012**, *12*, 4025−4031.

(59) McCann, R.; Roy, S. S.; Papakonstantinou, P.; Ahmad, I.; Maguire, P.; McLaughlin, J. A.; Petaccia, L.; Lizzit, S.; Goldoni, A. *Diamond Relat. Mater.* **2005**, *14*, 1057−1061.

(60) Kapteijn, F.; Moulijn, J. A.; Matzner, S.; Boehm, H. P. *Carbon* **1999**, *37*, 1143−1150.

(61) Zuckmantel, M.; Kurth, R.; Boehm, H. *Z. Naturforsch., B: J. Chem. Sci.* **1979**, *34*, 188−196.

(62) Clauss, A.; Boehm, H. P.; Hofmann, U. *Z. Anorg. Allg. Chem.* **1957**, *290*, 35−51.

(63) Carlsson, J. M.; Scheffler, M. *Phys. Rev. Lett.* **2006**, *96*, 0468061−0468064.

(64) Arrigo, R.; Haevecker, M.; Wrabetz, S.; Blume, R.; Lerch, M.; McGregor, J.; Parrott, E. P. J.; Zeitler, J. A.; Gladden, L. F.; Knop-Gericke, A.; Schlögl, R.; Su, D. S. *J. Am. Chem. Soc.* **2010**, *132*, 9616−9630.

(65) Stöhr, J. *NEXAFS Spectroscopy*; Springer: New York, 1992; Vol. 25.

(66) Yeh, J. J.; Lindau, I. *At. Data Nucl. Data Tables* **1985**, *32*, 1−155.

(67) Balmes, O.; Resta, A.; Wermeille, D.; Felici, R.; Messing, M. E.; Deppert, K.; Liu, Z.; Grass, M. E.; Bluhm, H.; van Rijn, R.; Frenken, J. W. M.; Westerström, R.; Blomberg, S.; Gustafson, J.; Andersen, J. N.; Lundgren, E. *Phys. Chem. Chem. Phys.* **2012**, *14*, 4796−4801.

(68) Schauermann, S.; Nilius, N.; Shaikhutdinov, S.; Freund, H. J. *Acc. Chem. Res.* **2013**, *46*, 1673−1681.

(69) Wilde, M.; Fukutani, K.; Naschitzki, M.; Freund, H. J. *Phys. Rev. B: Condens. Matter Mater. Phys.* **2008**, *77*, 113412.

(70) Doyle, A. M.; Shaikhutdinov, S. K.; Jackson, S. D.; Freund, H. J. *Angew. Chem., Int. Ed.* **2003**, *42*, 5240−5243.

(71) Kovnir, K.; Ambruster, M.; Teschner, D.; Venkov, T.; Szentmiklósi, L.; Jentoft, F. C.; Knop-Gericke, A.; Grin, Y.; Schlögl, R. *Surf. Sci.* **2009**, *603*, 1784−1792.

(72) Teschner, D.; Borsodi, J.; Wootsch, A.; Revay, Z.; Havecker, M.; Knop-Gericke, A.; Jackson, S. D.; Schlogl, R. *Science* **2008**, *320*, 86−89.

(73) Studt, F.; Abild-Pedersen, F.; Bligaard, T.; Sorensen, R. Z.; Christensen, C. H.; Norskov, J. K. *Science* **2008**, *320*, 1320−1322.

(74) Pallassana, V.; Neurock, M. *J. Catal.* **2000**, *191*, 301−317.

(75) Garcia-Lastra, J. M.; Cook, P. L.; Himpsel, F. J.; Rubio, A. *J. Chem. Phys.* **2010**, *133*, 151103(4).

(76) Blyholder, G. *J. Phys. Chem.* **1964**, *68*, 2772.

(77) Purans, J.; Fourest, B.; Cannes, C.; Sladkov, V.; David, F.; Venault, L.; Lecomte, M. *J. Phys. Chem. B* **2005**, *109*, 11074−82.

(78) Teschner, D.; Rèvay, Z.; Borsodi, J.; Hävecker, M.; Knop-Gericke, A.; Schlögl, R.; Milroy, D.; Jackson, S. D.; Torres, D.; Sautet, P. *Angew. Chem., Int. Ed.* **2008**, *47*, 9274−9278.

(79) Borodzinski, A.; Bond, G. C.; Nishimura, S. *Catal. Rev.: Sci. Eng.* **2008**, *50*, 379−469.

(80) Nishimura, S. *Handbook of Heterogeneous Catalytic Hydrogenation for Organic Synthesis*; Wiley-Interscience: New York, 2001; pp Vol. *148*.

(81) Wowsnick, G.; Teschner, D.; Armbrüster, M.; Kasatkin, I.; Girgsdies, F.; Grin, Y.; Schlögl, R.; Behrens, M. *J. Catal.* **2014**, *309*, 221−230.

(82) Rajaram, J.; Narula, A. P. S.; Chawla, H. P. S.; Dev, S. *Tetrahedron* **1983**, *39*, 2315−2322.

(83) Duprat, F. *Chem. Eng. Sci.* **2002**, *57*, 901−911.

(84) Engel, T.; Ertl, G. *J. Chem. Phys.* **1978**, *69*, 1267−1281.

(85) Ertl, G. *Science* **1991**, *254*, 1750−1755.

(86) Liu, R.; Wu, D.; Feng, X.; Muellen, K. *Angew. Chem., Int. Ed.* **2010**, *49*, 2565−2569.

(87) Lai, L.; Potts, J. R.; Zhan, D.; Wang, L.; Poh, C. K.; Tang, C.; Gong, H.; Shen, Z.; Lin, J.; Ruoff, R. S. *Energy Environ. Sci.* **2012**, *5*, 7936−7942.

(88) Shin, D.; Jeong, B.; Choun, M.; Ocon, J. D.; Lee, J. *RSC Adv.* **2015**, *5*, 1571−1580.